The Astrophysical Journal, 974:71 (15pp), 2024 October 10 https://doi.org/10.3847/1538-4357/ad6765
© 2024. The Author(s). Published by the American Astronomical Society.
OPEN ACCESS

CHIANTI—An Atomic Database for Emission Lines—Paper. XVIII. Version 11, Advanced Ionization Equilibrium Models: Density and Charge Transfer Effects

R. P. Dufresne[1], G. Del Zanna[1], P. R. Young[2,3], K. P. Dere[4], E. Deliporanidou[1], W. T. Barnes[2,5], and E. Landi[6]
[1] DAMTP, Center for Mathematical Sciences, University of Cambridge, Wilberforce Road, Cambridge, CB3 0WA, UK
[2] NASA Goddard Space Flight Center, Code 671, Greenbelt, MD 20771, USA
[3] Northumbria University, Newcastle Upon Tyne, NE1 8ST, UK
[4] Department of Physics and Astronomy, George Mason University, 4400 University Drive, Fairfax, VA 22030, USA
[5] Department of Physics, American University, Washington, DC 20016-8079, USA
[6] Department of Climate, Space Sciences and Engineering, University of Michigan, Ann Arbor, MI 48109, USA
Received 2024 March 19; revised 2024 July 9; accepted 2024 July 23; published 2024 October 4

Abstract

Version 11 of the CHIANTI database and software package is presented. Advanced ionization equilibrium models have been added for low charge states of seven elements (C, N, O, Ne, Mg, Si, and S), and represent a significant improvement especially when modeling the solar transition region. The models include the effects of higher electron density and charge transfer on ionization and recombination rates. As an illustration of the difference these models make, a synthetic spectrum is calculated for an electron pressure of 7×10^{15} cm^{-3} K and compared with an active region observation from HRTS. Increases are seen in factors of 2–5 in the predicted radiances of the strongest lines in the UV from Si IV, C IV, and N V, compared to the previous modeling using the coronal approximation. Much better agreement (within 20%) with the observations is found for the majority of the lines. The new atomic models better equip both those who are studying the transition region and those who are interpreting the emission from higher-density astrophysical and laboratory plasma. In addition to the advanced models, several ion data sets have been added or updated, and data for the radiative recombination energy loss rate have been updated.

Unified Astronomy Thesaurus concepts: Atomic data (2216); Atomic physics (2063); Solar ultraviolet emission (1533); Solar atmosphere (1477)

1. Introduction

The CHIANTI atomic database (Dere et al. 1997, 2023) is widely used in astrophysics to model line emission across the wavelength spectrum, but it is also increasingly used to model laboratory, high-density plasma (see, e.g., Kambara et al. 2021; Träbert et al. 2022). Significant effort has been devoted in numerous releases to improve the atomic rates used to calculate the emissivities of the spectral lines emitted by the most important ions for astrophysics. CHIANTI is now the most widely used atomic database for solar physics and has become, in certain cases, the reference for other atomic databases in astrophysics. For example, the CLOUDY spectral synthesis code was recently updated (Chatzikos et al. 2023) to include the CHIANTI 10.0.1 atomic data.

The main aim of this CHIANTI release is to improve the ionization equilibrium calculations for complex ions forming in higher-density plasma. Higher density here means electron densities in the range 10^8–10^{13} cm^{-3} and temperatures in the range 10^4–6×10^5 K, conditions which are typically prevalent in the solar transition region. One principal assumption within CHIANTI from the beginning has been that the plasma is in ionization equilibrium, and the ion abundances have been precalculated assuming the so-called "coronal approximation" (e.g., Equation (24) of Del Zanna & Mason 2018). This assumes that, for ionization and recombination purposes, atoms and ions are entirely populated in their ground state. Many of the other key assumptions in the coronal approximation are suitable only for high-temperature, low-density plasma; however, even at typical electron densities of the quiet-Sun (QS) corona some of the assumptions break down. The problem is magnified further in the higher-density transition region (TR). Various effects have been invoked in atomic modeling over the years to improve the agreement between observations and theory for the TR, as discussed below.

The current missions observing the solar TR, the Interface Region Imaging Spectrometer (IRIS; De Pontieu et al. 2014) and the Spectral Imaging of the Coronal Environment (SPICE; Consortium et al. 2020) spectrometer on the Solar Orbiter, observe many lines emitted by, e.g., C II, O II, O IV, O VI, Si IV, and S IV. These are used for a wide range of plasma diagnostics, but all show discrepancies between observations and theory. Although often not a physical representation of the plasma emission, since the 1960's various emission measure techniques were applied to observations. With the above simple assumption of ionization equilibrium and the coronal approximation, it was found that much of the plasma emission could be well represented, except several so-called "anomalous" ions from the Li- and Na-like sequences, such as C IV, O VI, and Si IV. These are underpredicted by typically a factor of 5 compared to those from other ion sequences that form at similar temperatures (see, e.g., Burton et al. 1971; Dupree 1972).

The main anomalous ions, such as Si IV, C IV, N V, and O VI, emit some of the strongest lines in the UV and the discrepancies have limited their potential use for plasma diagnostics. For example, to use the Si IV 1402.77 Å to O IV 1401.16 Å ratio for density diagnostics in flares from IRIS, Young et al. (2018) applied an empirical correction factor of 3

Original content from this work may be used under the terms of the Creative Commons Attribution 4.0 licence. Any further distribution of this work must maintain attribution to the author(s) and the title of the work, journal citation and DOI.

to the Si IV line intensity. Doschek & Mariska (2001) noted that the Si IV and O IV lines form at different temperatures (6.3×10^4 K and 1.6×10^5 K, respectively, using the coronal approximation), which makes it difficult to derive diagnostics from such lines. Young et al. (2018) and Doschek & Mariska (2001) both used CHIANTI for their modeling. Young et al. (2018) included a modification of the coronal approximation by applying an estimate of the suppression of dielectronic recombination (DR) at higher densities. This is a physical effect first noted by Burgess & Summers (1969) and was included in the ion balances of Jordan (1969) and Summers (1974), for instance.

Another improvement for the atomic models of Si and O was found by including charge transfer (CT). Charge transfer occurs during atom–ion or ion–ion collisions when an electron is exchanged between the colliders. Although O is usually only affected by this process in the solar chromosphere, Baliunas & Butler (1980) showed how all the Si ions forming in the solar transition region are affected. As an example, they estimated that the formation temperature of the Si III intercombination line at 1892.03 Å is 20,000 K when charge transfer is included, compared to 32,000 K predicted by the coronal approximation.

The problem of anomalous ions is present also in stellar atmospheres, as shown by Del Zanna et al. (2002), where EUV and UV observations from several satellites were combined. Sim & Jordan (2005) included an approximate treatment of DR suppression and CT for some ions in their semiempirical atmospheric models for ϵ ERI (K2 V), apparently resolving the main discrepancies.

One further improvement used in the atomic modeling is to account for ionization and recombination from metastable levels. These longer-lived levels become populated in higher-density plasma, which alters the ionization and recombination rates of the ion. The importance of this was first demonstrated by Nussbaumer & Storey (1975), who showed that all the carbon ions in the transition region are formed at lower temperatures than in the coronal approximation. They showed the effect on temperature and density diagnostics for a range of solar conditions when using the C II 1334.53 Å line, which is also observed by IRIS, but note that ions of all elements forming in the transition region should be affected by this process. An approximate treatment of both DR suppression and ionization from metastable levels plus charge transfer was developed by J. Raymond, as briefly described in Vernazza & Raymond (1979). In a follow-up paper, Raymond & Doyle (1981) applied a differential emission measure (DEM) method to Skylab observations of the QS, apparently resolving the main discrepancies, without invoking time-dependent ionization or other effects.

All of the above-described improvements to the atomic modeling were integrated recently, with updated atomic rates, into models for the main elements observed in the solar transition region (C, N, O, Ne, Mg, Si, and S), as described in Dufresne & Del Zanna (2019) and Dufresne et al. (2020, 2021a, 2021b). Significant changes were observed in the ion balances at typical densities from the QS through to flares, especially below 10^5 K. A comparison of these models with results from the coronal approximation and with a compilation of averaged intensities of the QS (Dufresne et al. 2023) showed significant improvements. Changes in predicted intensities by factors of 2 were shown in a number of cases, such as the O II 718.49 Å lines observed by SPICE. The intensities of the Si IV resonance lines were enhanced by a factor of 6, bringing the ratio with the O IV intercombination lines much closer to observations. However, some discrepancies with observations for the anomalous ions were still present.

Of course, changes to the atomic modeling are not the only effects that could bring improved agreement. While atomic modeling is known to particularly affect Li- and Na-like ions, an investigation by Judge et al. (1995) considered this insufficient to entirely account for the discrepancy in these ions. Judge et al. (1995) and other authors have suggested that the main cause of the discrepancy could be the assumption of ionization equilibrium (such as Pietarila & Judge 2004; Olluri et al. 2013). Time-dependent ionization is at play whenever the timescales for ionization and recombination of an ion are longer than those of the processes affecting the plasma state. Also, photoionization can affect significantly the charge states, depending on the ion and conditions. Atoms and singly or doubly charged ions can be affected by opacity and a full radiative transfer might need to be performed (such as Rathore & Carlsson 2015). Finally, Dudík et al. (2014) pointed out, instead, that non-Maxwellian electron distributions could also explain the Si IV to O IV anomaly in the IRIS spectra.

The remainder of this paper describes the improvements made to the atomic modeling in CHIANTI for the current release. The next section of this article describes in more detail the atomic processes being included and the various approximations used to incorporate them. Section 3 gives examples of how the new models compare with the coronal approximation. It presents a comparison with observations from HRTS of an active region (AR) using DEM modeling to show the improvements over the coronal approximation. A section describing other updates to the database follows in Section 4. A short conclusion is given at the end.

2. Advanced Models for Medium- to High-density Plasma

In this section, we describe the atomic processes and methods used for the new advanced models. The implementation is simpler than that used by Dufresne & Del Zanna (2019) and Dufresne et al. (2020, 2021a, 2021b), and only the ionization fractions are affected in comparison to the previous CHIANTI models. The new methods do not impact level populations. The models are currently only available for ions of C, N, O, Ne, Mg, Si, and S. The new models are switched on by default in the CHIANTI IDL software, but they can be switched off using the setting "`advanced_model = 0`" if preferred. The advanced models are not currently implemented in ChiantiPy.

One key assumption we retain in the present modeling is that the timescales for ionization/recombination, which are related to the electron density, are such that the plasma is in ionization equilibrium. To assess the applicability of ionization equilibrium, we can consider the timescales of some of the more rapidly evolving features in the solar atmosphere. Type II spicules in chromospheric lines were found by de Pontieu et al. (2007) to have lifetimes in the range of 10–60 s. If the same features were to extend into the transition region, then at the typical AR densities used in the present work the ionization and recombination timescales of C II at its peak formation temperature are 580 s and 2 s, respectively, for S III they are 11 s and 0.5 s respectively, and for C IV they are 16 and 0.3 s. This indicates that for a cooling plasma in such rapid events, where recombination is the dominant process, ionization

equilibrium is likely to hold, while for a heating plasma, it is possible that enhanced emission may occur in a low-charge state before ionization takes place. Given that these are some of the fastest-evolving events, however, it would appear that ionization equilibrium is a reasonable assumption for many of the structures in the solar transition region.

The models included in the present version of CHIANTI use the rates as described in the works referenced above. Those works tested as many atomic effects as possible, which were likely to influence ion fractions in these conditions. Those tested but found to not be important for ion formation were: inelastic collisions with hydrogen, collisional ionization ejecting two or more electrons, stimulated emission and photoexcitation, stimulated radiative recombination, and three-body recombination. Other processes affecting plasma at higher densities than the range of interest here, such as ionization potential depression and free–free heating, were not investigated. (Photoexcitation was shown to affect level populations of neutrals and some singly charged ions in the solar atmosphere, and is already included in CHIANTI for that purpose, but it does not affect the ion balances. Photoionization was found to be important for low-charge states and will be included for these models in a future CHIANTI release.) We provide now a brief description of the processes that have been included in the present models.

2.1. Collisional Ionization

Atomic energy levels that have no rapid, dipole-allowed decay to lower energy levels can become significantly populated in certain conditions. For instance, in high electron densities, they become populated through the balance of collisional excitation and deexcitation. Such energy levels are denoted as metastable levels. Rate coefficients for collisional ionization from metastable levels are generally larger than those from the ground level in the same ion because metastable levels are closer to the continuum. The overall ionization rate coefficient out of the ion is the sum of the total ionization rate coefficient from each initial level weighted by the relative population of the level. When metastable levels become populated in higher-density plasma the overall ionization rate coefficient is higher than in a low-density plasma. This causes the ions to form at lower temperatures. The coronal approximation only includes ionization from the ground level and cannot take this effect into account.

2.1.1. Sources of Rate Coefficient Data

The collisional ionization rates for the ground and metastable states of carbon and oxygen were calculated in Dufresne & Del Zanna (2019) and Dufresne et al. (2020), respectively. FLEXIBLE ATOMIC CODE (FAC; Gu 2008) was used for direct collisional ionization and AUTOSTRUCTURE (Badnell 2011) for excitation–autoionization (or indirect collisional ionization). The cross sections were benchmarked against many of the same experiments as Dere (2007), whose ground-level collisional ionization rates have been used in CHIANTI for the default ion balances until now. To provide a consistent set of rates for the advanced models, the rate coefficients from Dufresne & Del Zanna (2019) and Dufresne et al. (2020) are used for ground and metastable levels of carbon and oxygen.

For other ions included in the advanced models, the same method is used as Dufresne et al. (2021b). The rate coefficients of Dere (2007) are used for the ground levels. To estimate rates for metastable levels, the Burgess & Chidichimo (1983) collisional ionization approximation for low-charge ions is used to calculate the ratio of the metastable-to-ground rate coefficients. The Dere (2007) rate coefficients are multiplied by this ratio to estimate those for the metastable levels. The ionization potentials required by the Burgess & Chidichimo (1983) approximation are taken from experimental values stored in CHIANTI for each ion. Dufresne et al. (2021b) compared the oxygen ion balance obtained using this approximation with that obtained using ab initio collisional ionization rate coefficients; differences in the ion balance were negligible.

2.1.2. Calculating Overall Ionization Rates for Neutrals

To obtain overall ionization and recombination rates for the models requires knowing the level populations within each ion (see Section 2.4 for more details). Radiative decay and electron impact excitation rates are needed to determine this. CHIANTI 10.1 had rates for all ions of C, N, O, and S, but for Ne, Mg, and Si CHIANTI did not have the neutral atom. So, it has been necessary to create new models. The Ne I model represents a new addition to the regular database. Only approximate models could be constructed for Mg I and Si I which are not suitable for computing accurate line emission. Therefore, although the data files have been added to the database, the ion names have been omitted from the CHIANTI "masterlist" file for the latter two ions. (The CHIANTI User Guide provides more detail on how ions in the "masterlist" are treated.)

For Ne I energies and radiative decay rates are taken from the energy-adjusted calculation of Froese Fischer & Tachiev (2004), as made available on the NIST MCHF collection website.[7] Excitation data are taken from the B-spline *R*-Matrix calculation of Zatsarinny & Bartschat (2012a) in *jK* coupling and were made available by Professor Bartschat (2024, private communication). Since all the data are obtained from ab initio calculations the data are suitable for spectroscopic analysis of this ion.

All data in CHIANTI are resolved by fine structure, but the only available excitation data for Mg I, from Barklem et al. (2017), are in *LS* coupling. In cases where resolution by fine structure is required in the data, transitions involving multiplets are often split according to the statistical weights of the levels. This approach is very approximate and relevant only for plasma in which densities are high enough that energy levels within a term are populated according to statistical weight. Another way of splitting the data was tested here. AUTOSTRUCTURE (AS) was used to calculate excitation data for Mg I in intermediate coupling. The *LS* coupling data of Barklem et al. (2017) was split into the same ratios as the AS intermediate coupling data for the levels within each term. This second approach was found to be preferable because it accounts for the relative strengths of the transitions within a multiplet seen in the intermediate coupling data, rather than distributing them purely by statistical weight. (AS cannot be used in itself for the neutral excitation data because it implements the distorted wave method, which is known to be insufficiently accurate compared to nonperturbative methods for low-charge ions).

As a result of splitting the rates, the data for Mg I should be used only for calculating metastable ionization and

[7] https://nlte.nist.gov/MCHF/

recombination, which is not as sensitive to accuracy in level populations as high-resolution spectroscopy. There are two types of excitation data in Barklem et al. (2017); the B-spline *R*-Matrix excitation data were used here, as provided by Professor Bartschat (2024, private communication). Again, level energies and radiative data were taken from Froese Fischer & Tachiev (2004), but this time using the ab initio, not energy-adjusted, data because more transitions were included.

The same simple model for Si I is used as in Dufresne et al. (2021b). This used energy levels and radiative data from Fischer (2005), supplemented by additional radiative data from a calculation using ATSP2K (Froese Fischer et al. 2007). As above, since the excitation data came from a distorted wave calculation, it is strongly recommended that the data for this ion are not used for any purpose other than calculating overall ionization and recombination rates.

2.2. Radiative and Dielectronic Recombination

Since metastable levels are further away in energy than the ground from levels in the next lower charge state, rate coefficients for radiative recombination (RR) and DR are generally smaller for metastable levels than the ground. This will also cause ions to form at lower temperatures when metastable levels become populated compared to the coronal approximation.

2.2.1. Sources of Rate Coefficient Data

We use the RR rate coefficients calculated by Badnell (2006). The DR rate coefficients for the ground and metastable levels have so far been calculated for all ions of hydrogen to zinc in the H-like to P-like isoelectronic sequences by the DR Project (see Badnell et al. 2003, for the first paper in the series). The rate coefficients are available for all ground and metastable levels up to the first dipole-allowed transition in the ion. Previous versions of CHIANTI only included the RR and DR rate coefficients for ground levels, using the fitting coefficients made available by N.R. Badnell.[8] We now include in CHIANTI the RR and DR rates for metastable levels using the same set of data. Rate coefficients were calculated to final resolved states at zero density in those works; here, we use total rate coefficients resolved by the initial level to the next lower charge state.

2.2.2. Dielectronic Recombination Suppression

DR mostly goes through highly excited, Rydberg levels close to the continuum. In higher-density plasma these levels are rapidly ionized by free electrons before decays to lower levels take place. The effects are not easy to calculate, as they require complex collisional–radiative models and a large number of rates, which are not easy to calculate accurately. Simple hydrogenic models with very approximate atomic rates were developed by Burgess & Summers (1969, 1976). The tables of the resulting effective recombination rates obtained by Summers (1974) have then been used by the authors previously mentioned (Jordan 1969; Vernazza & Raymond 1979; Judge et al. 1995) to approximate DR suppression.

In a recent version of CHIANTI (v10; Del Zanna et al. 2021), the Nikolić et al. (2018) approximation for DR suppression was introduced. This has been used in the present advanced models to reduce the DR rates for both the ground and metastable

[8] http://apap-network.org/

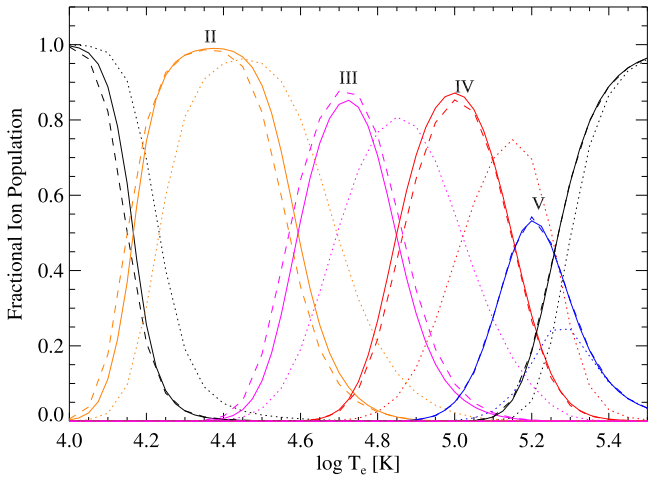

Figure 1. Comparison of the effect of different approximations for DR suppression on the nitrogen, density-dependent ion balance of Dufresne et al. at 10^{12} cm^{-3} density: solid line—using DR suppression from Summers tables, dashed—using DR suppression from Nikolić et al. (2018, dotted)—coronal approximation. Ions are indicated by Roman numerals for the effective ion charge and by different colors.

levels. Although the same ionization and recombination rates are being used for the present models as Dufresne et al. (2021b) and the preceding works, those works use DR suppression factors derived from the Summers (1974) tables. The differences in ion fractions produced by these two methods are generally small, as illustrated in Figure 1 for nitrogen. Differences between the two methods have only been assessed for elements included in the advanced models, and so DR suppression is not switched on for other cases. The user can add it for all elements by using the "`dr_suppression`" keyword if desired.

2.3. Charge Transfer and Associated Model Atmospheres

Another physical effect that changes significantly the ion balance for some ions in the chromosphere and TR is CT during collisions with the most abundant species: hydrogen and helium. CT is the exchange of an electron that takes place between two colliders during atom–ion or ion–ion collisions. The process is variously known as charge transfer, charge exchange, and electron capture. Baliunas & Butler (1980) demonstrated that silicon is strongly affected in the solar atmosphere, but it was only relatively recently that more accurate, quantum-mechanical calculations became available, many of which included rates for metastable levels. Earlier calculations used the rather approximate Landau–Zener method, but its assumptions are more suitable for higher collision energies (Bates & McCarroll 1962).

Dufresne et al. (2021a) and Dufresne et al. (2021b) made a comparison of all CT cross sections available for the low-charge ions of the elements being modeled. Preference was given for results from more accurate methods and those that included metastable levels. Rate coefficients were calculated from the cross sections if not published in the original articles. All except one calculation was in *LS* coupling, and rate coefficients were split according to statistical weights of the initial levels in each term; ground and metastable levels are populated in these ratios for all the ions under consideration in the solar TR. Double electron capture is also possible and was

included in the earlier models, but the ion balances were not affected by this and it has been neglected in CHIANTI.

The CT rate also depends on the number density in the plasma of the relevant perturber, atomic or ionized hydrogen or helium in this case, and its ion fractions. Self-consistent calculations of these values are not feasible and they are usually taken from model atmosphere calculations. The relevant number densities from the model atmospheres are interpolated in temperature over the temperature grid required for the ion balance. Model atmospheric data can be tabulated by the user and read in for the calculation. A number of files have been prepared for the present version, including those of Avrett & Loeser (2008) and Fontenla et al. (2014); data from the latter include the QS, an AR, plage, and facula.

2.4. Solving the Ion Balances

One of the main differences here compared to the earlier TR models is the solution of the ion balances. The earlier models included in one large matrix all the rates connecting the metastable levels to the ground states of the lower and higher charge states, plus all the rates required within each ion. The matrix was then inverted to find the populations of all the levels of all the charge states at once. We adopt here a simplified, faster method.

In Dufresne et al. (2021a) the level populations were solved using models in which collisional ionization and CT were fully level-resolved. In densities typical of the solar TR, they found that the level populations were all within 2% of the level populations from the CHIANTI independent atom model, except one level in O II which had a difference of 7%. This is because, for the main lines under consideration in the advanced models, collision rates between levels in an ion are much faster than processes connecting ions. This means in these conditions total collisional ionization and CT rates can be used, that is, rates that are resolved only by the initial level and not the final level. Dufresne et al. (2021a) and the other related models used total RR and DR rates. Level populations can be affected by level-resolved RR and DR, but such models are too large and complex to be included in the CHIANTI models. The issues associated with such models can be found in Del Zanna et al. (2020) for example.

These conditions allow the independent atom model already implemented in CHIANTI to be exploited. The level populations within each ion are calculated first to find the ground and metastable populations. From these, overall ionization and recombination rates out of the ion can be calculated. For example, if S_i is the ionization rate from level i, which has a fractional population n_i, then the overall ionization rate out of the ion is

$$S = \sum_i n_i S_i \,, \tag{1}$$

where the sum is over all metastable levels. This replaces S_g, the total ionization rate from the ground level, used to solve the coronal approximation ion balance.

An example is given in Figure 2 of how the overall ionization rates change as metastable levels become populated. The rates are shown for the low-charge states of carbon using a constant pressure of 7×10^{15} cm^{-3} K, which is the value used below for a solar AR. The figure shows the ratio of various values in the advanced models to the values from the coronal models; the quantities illustrated are: ground term populations, overall ionization, and overall recombination rates. Taking C II, for instance, it is seen that as temperature increases and the $2s\,2p^2\,{}^4P$ metastable term population increases to 20% the overall ionization rate out of the ion increases by 20%–40%. A corresponding decrease can be seen in the overall recombination rate into neutral carbon once the metastable term becomes populated. At low temperatures, despite the metastable levels not being populated, the ratio for the C II recombination rate is less than one because DR suppression has an effect on the higher densities present in the solar atmosphere. There are no metastable levels in C IV and so the ionization rate ratio is one at all temperatures. The recombination rate ratio is flat for the same reason; however, the value is not one because DR suppression is important during recombination into C III. The enhancements for the overall ionization rates out of C I and C III are large, being in the range 2–3 for the temperatures at which they form. The reason why the ionization rate ratio decreases as the metastable term population increases for these ions is that the ground and metastable ionization rates become closer as temperature increases, thus reducing the relative enhancement in the advanced model.

For neutrals, the CHIANTI routine "`metastable_levels`" is used to define the levels for which ionization data are included. In the routine, metastable levels are defined as those levels for which there is no decay rate above 10^5 s^{-1}. For ions, however, the only metastable levels included in the overall rates are those for which recombination data have been calculated (see Section 2.2 for the criteria). The ions included in the advanced models are given in a new master list. For all other ions it is assumed, as previously, that the population is in the ground state for ionization and recombination purposes, and there is no suppression of DR rates with density.

Once the overall rates are calculated, the same method previously used in CHIANTI to calculate the ion populations is used. Essentially, the ratio of the populations of two successive charge states is proportional to the ratio of the ionization/recombination rates. We have verified that the large matrix approach and the independent atom model produce the same ion abundances, within a fraction of a percent. The ion charge states can be both calculated on the fly and stored in CHIANTI format files for later use. The IDL software has been modified to calculate the advanced ion models by default, and a program has been provided to compare different ionization equilibria. More details are provided in the software notes.

3. Examples of Ion Balances and Comparison with Solar Observations

It is well known that the greatest effects on ion balances are found at high electron densities, particularly in the Si IV, C IV, and N V lines emitted in the transition region (see Doyle et al. 2005, for example). To illustrate the effects of the advanced models we create synthetic spectra for an AR using the new and existing models in CHIANTI, and then compare them with solar observations of an AR. Throughout, we choose these simple assumptions for the modeling: the plasma is in ionization equilibrium; its temperature distribution can be modeled with a DEM that is a single-valued function of the temperature; the atmosphere is static and fills the volume. Another common assumption for the TR is that of constant electron pressure. The model atmosphere data made available here from radiative transfer calculations with a static atmosphere show almost constant electron pressure through the TR,

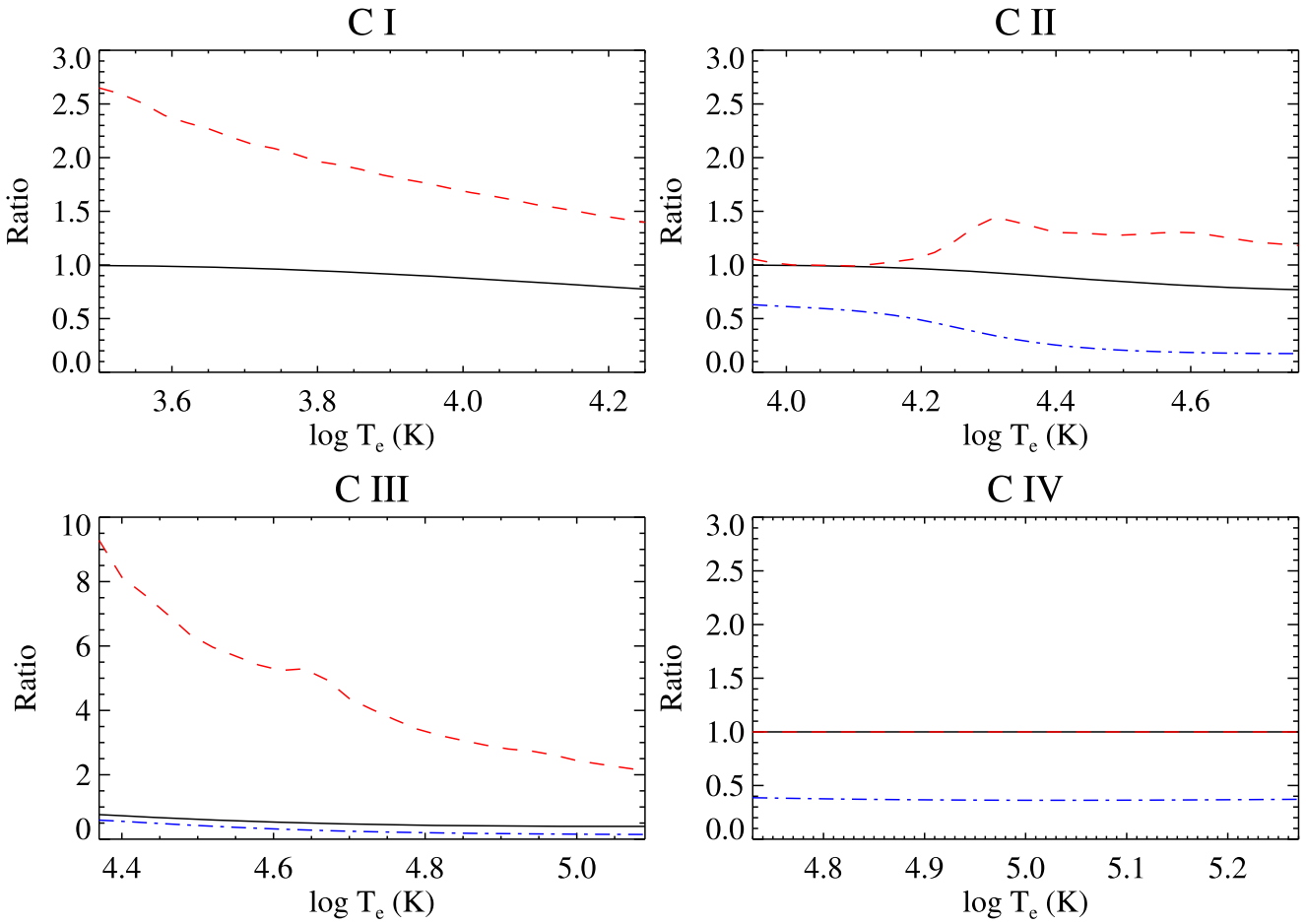

Figure 2. Ratios of various quantities in the advanced model to the same values in the coronal model for C I–IV at a constant pressure of 7×10^{15} cm^{-3} K. The quantities are ground term population (solid black line), overall ionization rate to the next higher charge state (red dashed), overall recombination rate to the next lower charge state (blue dashed–dotted). There is no recombination from C I and the ratios for the changes in ground term population and overall ionization rate out of C IV are unity at these temperatures.

and so we also use this in the present analysis. The pressure used is 7×10^{15} cm^{-3} K, as determined from the observations and detailed in Section 3.2.1 below. In the ion balances, we use the Fontenla et al. (2014) facula model atmosphere for the CT data because its pressure throughout the TR matches the pressure determined from the observations.

We acknowledge that, in reality, the solar transition region is actually highly dynamic, such that time-dependent ionization can be important, and the physical structure of the emission is possibly highly filamentary. For this reason, proper modeling of the TR is a complex matter, but the present assumptions are still widely used in the literature and will suffice for the simple comparison provided here. We present the ion balances first to highlight what the new, improved models look like and to help explain the changes they cause in line emission. Following that, we describe the methods used for comparing synthetic line intensities with observations and then present the results.

3.1. Ion Balances

Figure 3 shows the new ion fractions calculated at the selected pressure compared to the zero density CHIANTI v.10.1 models for the Si, C, N, O, Ne, and S ions of relevance here. The plots illustrate the fact that TR ion formation is generally shifted toward lower temperatures. This is caused by ionization and recombination from metastable levels in combination with DR suppression. The peaks of the Li- and Na-like, anomalous ions, especially C IV, N V, and Si IV, are clearly enhanced. The peak in the ion fractions increases for most other ion sequences, although not to the same extent. The shifts to lower temperatures usually cause lines that form at lower temperatures to be enhanced relative to lines in the same ion that form at higher temperatures. Thus, intensity ratios for lines that are emitted by the same ion can also be affected by the ion balances, and not solely by transitions within an ion.

Carbon and neon are unaffected by charge transfer, while it primarily affects nitrogen, oxygen, and sulfur in the chromosphere, as highlighted by Figure 3. By contrast, it is well known from the literature that all TR ions of Si are significantly affected by CT. The ion balance for Si in Figure 3 shows that ion formation shifts to a much lower temperature and Si IV forms over a much wider temperature range.

Inevitably, different atmospheric models will affect the ion balances when CT has an influence because CT rates depend on the total number densities and ion fractions of H and He taken from the model atmospheres. When different model atmospheres within the same work were chosen, such as the QS and AR plage from Fontenla et al. (2014), the ion fractions for Si II and Si III changed by 10% at the most compared to using the facula model from the same work. However, we show the effects on the ion balances in Figure 4 that can be obtained when using data from entirely different works. These are an AR facula from

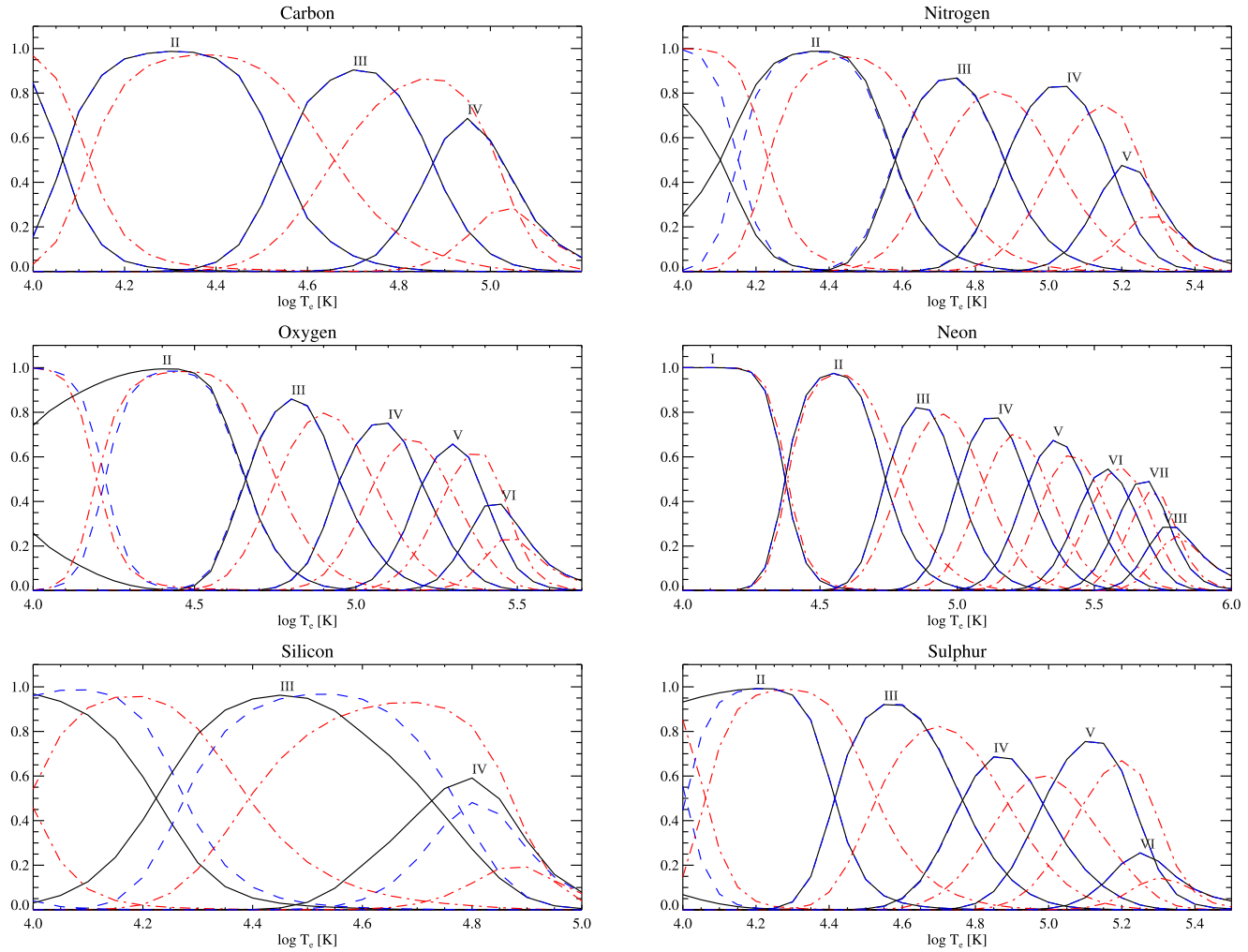

Figure 3. Ion balances calculated with the present advanced models at a constant electron pressure of 7×10^{15} cm^{-3} K, with CT included using the Fontenla et al. (2014) facula model atmosphere (black solid lines). We also show the advanced models without charge transfer (blue dashed lines) and the CHIANTI v.10.1 coronal approximation model (red dashed–dotted lines).

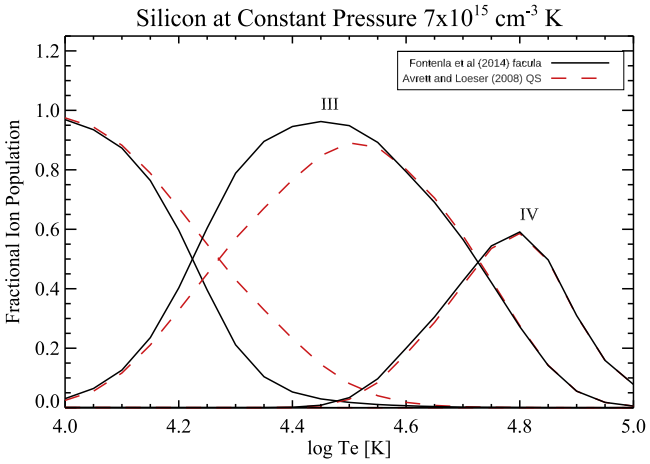

Figure 4. Ion balances calculated with the present advanced models at a constant electron pressure of 7×10^{15} cm^{-3} K, with CT included, with the Fontenla et al. (2014) facula model atmosphere and that of the QS from Avrett & Loeser (2008). Note that the main Si III lines are formed near $\log T = 4.6$ where differences are small.

Fontenla et al. (2014) and the QS model from Avrett & Loeser (2008). The main effect is caused by CT ionization and recombination between Si II and Si III during collisions with H.

Collisions with helium affect the ion balance between Si III and Si IV. In both ion balances shown in Figure 4, the default He fractions from CHIANTI were used because neither of the model atmospheres provided He data. Despite this, tests using the He model of Del Zanna et al. (2020), which in some cases had He ion fractions significantly different than CHIANTI, produced changes in ion formation of less than 10%. Even with the differences in the ion fractions caused by the model atmospheres, it is noted that the main Si III and Si IV lines in the High-Resolution Telescope and Spectrograph (HRTS) wavelength range have contribution functions that peak at temperatures higher than the peak in the ion abundance. So, the choice of the atmospheric model does not affect the calculated line intensities for these ions, as discussed below.

Neon is not affected by CT, but Dufresne et al. (2021b) showed that it was the element most affected by photoionization, which should be considered when modeling ions up to Ne IV because it is not currently implemented in CHIANTI. All the TR ions of Ne are shifted to lower temperatures and higher peak ion fractions in the advanced models, although the changes are smaller than those seen for O. Figure 3 shows that S I, like Si I, is significantly depleted in the chromosphere. For the S ions which form in the TR the shifts to lower temperature and increases in peak ion fractions caused by level-resolved

Table 1
Results of the DEM Analysis of the HRTS-II Plage

Wavelength (Å)	I_{obs}	Ion	Adv. Models with CT		Adv. Models without CT		CHIANTI v.10.1	
			$\log T_{eff}$	I_{calc}/I_{obs}	$\log T_{eff}$	I_{calc}/I_{obs}	$\log T_{eff}$	I_{calc}/I_{obs}
1533.44	185	Si II	4.10	1.13	4.13	1.17	4.28	0.87
1264.74	276	Si II	4.15	0.70	4.18	0.79	4.40	0.82
1260.42	121	Si II	4.15	0.90	4.18	1.01	4.40	1.05
1259.52	67.2	S II	4.24	1.12	4.26	0.95	4.46	0.96
1253.81	53.0	S II	4.24	1.04	4.27	0.89	4.47	0.89
1250.58	37.4	S II	4.25	0.71	4.27	0.61	4.47	0.63
1194.45	134	Si II	4.26	1.06	4.28	1.22	4.46	1.38
1335.70	3450	C II	4.41	1.26	4.41	1.22	4.55	1.35
1334.53	2620	C II	4.41	0.85	4.42	0.82	4.56	0.93
1206.48	4920	Si III	4.55	0.83	4.59	0.90	4.64	0.82
1200.94	110	S III	4.60	0.97	4.61	1.00	4.69	0.82
1402.76	521	Si IV	4.73	1.10	4.78	0.70	4.91	0.23
1393.75	1500	Si IV	4.73	0.76	4.78	0.48	4.91	0.16
1247.39	16.7	C III	4.74	0.98	4.74	1.10	4.90	1.47
1423.84	5.15	S IV	4.82	1.07	4.81	1.17	4.95	0.96
1406.05	26.5	S IV	4.83	1.19	4.82	1.30	4.96	1.15
1550.79	1590	C IV	4.95	0.84	4.94	0.83	5.02	0.50
1548.21	3170	C IV	4.95	0.84	4.94	0.84	5.02	0.50
1486.51	31.4	N IV	5.02	0.93	5.02	0.93	5.08	0.96
1404.80	36.5	O IV	5.05	0.92	5.04	0.93	5.12	0.98
1407.38	26.9	O IV	5.07	1.28	5.08	1.24	5.12	1.34
1401.16	102	O IV	5.08	1.19	5.09	1.17	5.13	1.28
1199.17	46.9	S V	5.09	0.69	5.10	0.68	5.12	0.60
1238.82	240	N V	5.24	0.82	5.23	0.86	5.32	0.34
1218.35	203	O V	5.30	1.06	5.29	1.06	5.38	0.98

Note. I_{obs} is the measured intensity in erg cm^{-2} s^{-1} sr^{-1}.

ionization and recombination are reasonably large. Changes to Na-like S VI, however, are more modest than the other Li- and Na-like ions except for Ne VIII.

The only element in the advanced models for which the necessary CT data are not available is Mg; this is because there are no CT calculations that include metastable levels for the relevant ions. However, tests were carried out by Dufresne et al. (2021b) to assess whether the process affects this element. They used the coronal approximation and the rate coefficients from the compilation of Kingdon & Ferland (1996) and found that Mg I was almost completely ionized in the solar chromosphere in QS conditions. This obviously means Mg II is the dominant species in this region, although none of the higher charge states are affected by the process. Density-dependent effects on free-electron ionization and recombination have been included for Mg, although this affects Mg IV–X formation to a lesser extent than the changes shown in Figure 3 for the second row elements. Changes to the high charge states (Li- to F-like sequences) of Si and S are also relatively small.

3.2. Comparison with Observed Line Intensities

3.2.1. Observational Data Used

Of the lines from anomalous ions mentioned above, IRIS observes only the Si IV doublet and does not record enough lines to estimate the temperature distribution of the plasma. Aside from Skylab, SoHO SUMER observed these lines, but not simultaneously. The NRL HRTS was flown several times, observing the entire 1150–1600 Å region with an excellent resolution of 0.05 Å. For the present comparison with observations, we have chosen the HRTS-II spectra of an on-disk, AR plage, as provided by Brekke (1993).

We selected the main lines and measured their radiances with Gaussian fits. Although the profiles of the lines we selected are not self-reversed, the profiles are not exactly Gaussian. This issue combined with the complex conversion from plate density to radiometric calibration means that radiances have a possible uncertainty on the order of 30%. The main lines from Si IV, C IV, and N V do not show any opacity effects when considering the intensity ratios. However, the brightest line in the C II multiplet, at 1335.7 Å, appears to be partially affected by opacity because the intensity ratio of the lines within the multiplet differs from the optically thin limit.

The main diagnostics to measure the electron density within the HRTS wavelengths are given by the O IV lines. The 1399 Å line is generally very weak, while the 1406 Å line is blended with S IV. De-blending the 1406 Å line is preferable, as discussed by Rao et al. (2022). However, a better line available to HRTS is the 1407 Å line, in conjunction with the strongest O IV line at 1401 Å. This ratio indicates a density of 5×10^{10} cm^{-3} using the current data in CHIANTI, equivalent to a pressure of about 7×10^{15} cm^{-3} K, which is adopted here.

3.2.2. Methods Used to Calculate the Synthetic Spectra

We used the "`chianti_dem`" routine to calculate the DEM using the selection of lines shown in Table 1. We adopted the MPFIT method, which searches for the best solution having defined a set of DEM spline nodes and uncertainties; the uncertainties are assumed to be 30% based on the calibration, while the spline nodes were set at log temperatures (in Kelvin)

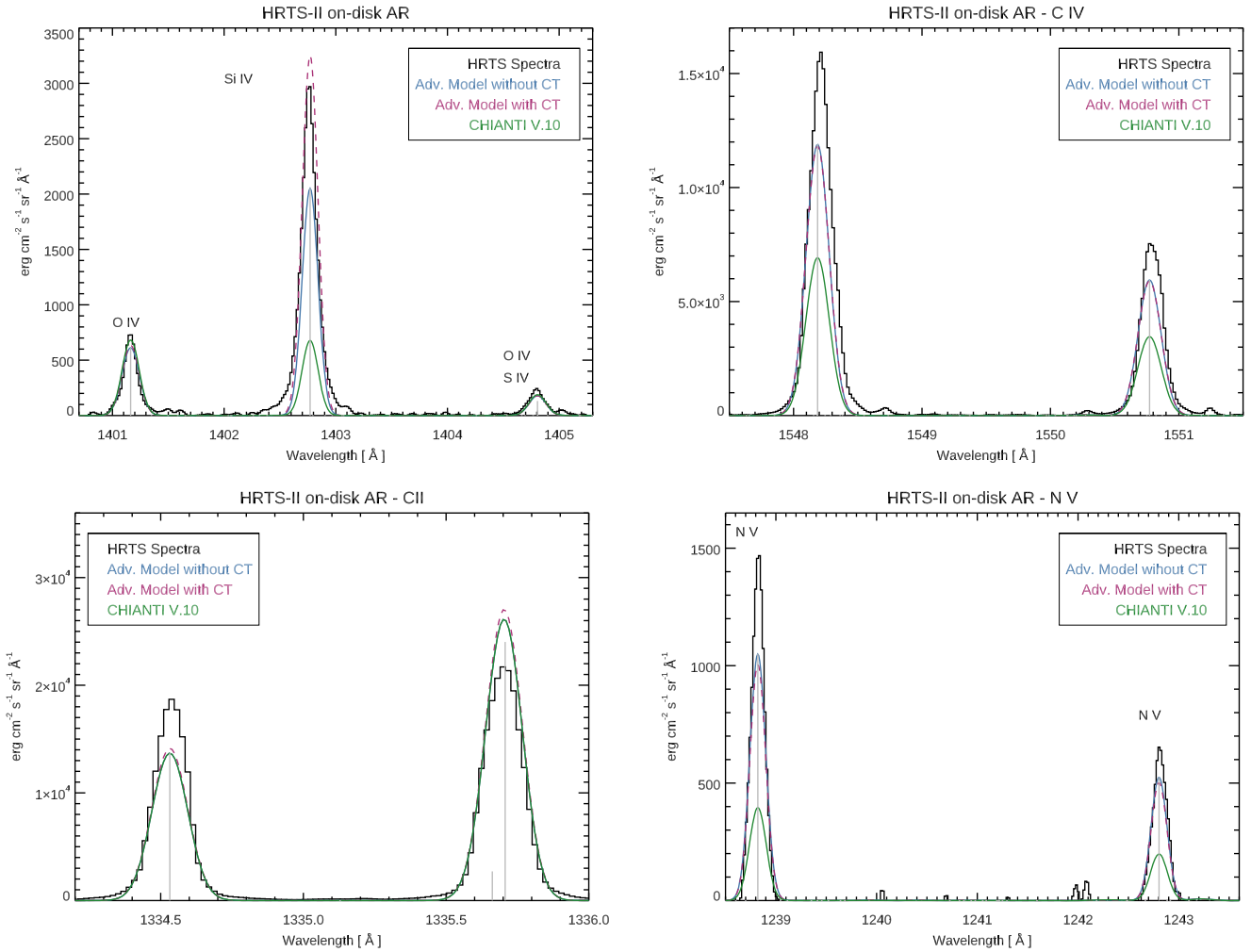

Figure 5. HRTS-II spectra of an on-disk AR plage, superimposed with various synthetic spectra calculated using the present advanced models at a constant electron pressure of 7×10^{15} cm^{-3} K. The synthetic spectrum obtained with the CHIANTI v.10.1 coronal approximation ion fractions are shown in green, that obtained from the advanced model without charge transfer is shown in blue, and that obtained with the advanced model including charge transfer is shown with a magenta dashed line. The theoretical wavelength for each transition is shown by a vertical gray line.

of 4.0, 4.3, 4.6, 4.8, 5.0, 5.2, 5.4, and 5.5. We made three calculations using the same input parameters (set of lines, elemental abundances, spline nodes) and only changed the ion balances in the input. We first ran the advanced model with charge transfer, obtaining good agreement within uncertainties between observed and predicted radiances. We then calculated the DEM using the advanced models without CT, to highlight which lines are most affected by this process. Finally, we ran everything again but used the coronal ion balances from CHIANTI v.10.1. The photospheric elemental abundances of Asplund et al. (2021) were used in all three cases. These methods mean that changes in the predicted line intensities can be understood entirely in terms of the changes seen in the ion balances in Section 3.1 and the DEMs derived from them.

Gaussian line profiles were used for the model spectra and the widths are the same for each line. Because changes in ion and line formation temperatures are important, we calculate the effective temperature $T_{\rm eff}$ defined by

$$T_{\rm eff} = \frac{\int G(T)\,{\rm DEM}(T)\,T\,dT}{\int G(T)\,{\rm DEM}(T)\,dT}.$$

This is an average temperature more indicative of where each line is formed because the line contribution function, $G(T)$, is weighted by the emission measure. It is noted that $T_{\rm eff}$ is generally different than the peak of the ion balance or the peak of the $G(T)$.

3.2.3. Results

Figure 5 shows four spectral ranges from the HRTS-II spectra with the three model spectra overplotted. Table 1 shows a summary of the measured radiances, the effective temperatures, and the ratios between predicted and observed values from the three different models. Figure 6 shows the resulting DEMs.

Lines from Si II and S II are included in the calculation only to constrain the DEM at low temperatures. Lanzafame (1994) showed in hydrostatic, radiative transfer calculations that the Si II lines are optically thick in all parts of the Sun, and so a DEM calculation will not produce meaningful results for these lines. Dufresne et al. (2023) found in the QS case that the S II lines were far from the emission measure of other lines forming at a similar temperature. Therefore, neither of these ions will be discussed further other than to say that there is reasonable consistency in the predicted to observed intensities for the lines, which was not the case in the QS observations.

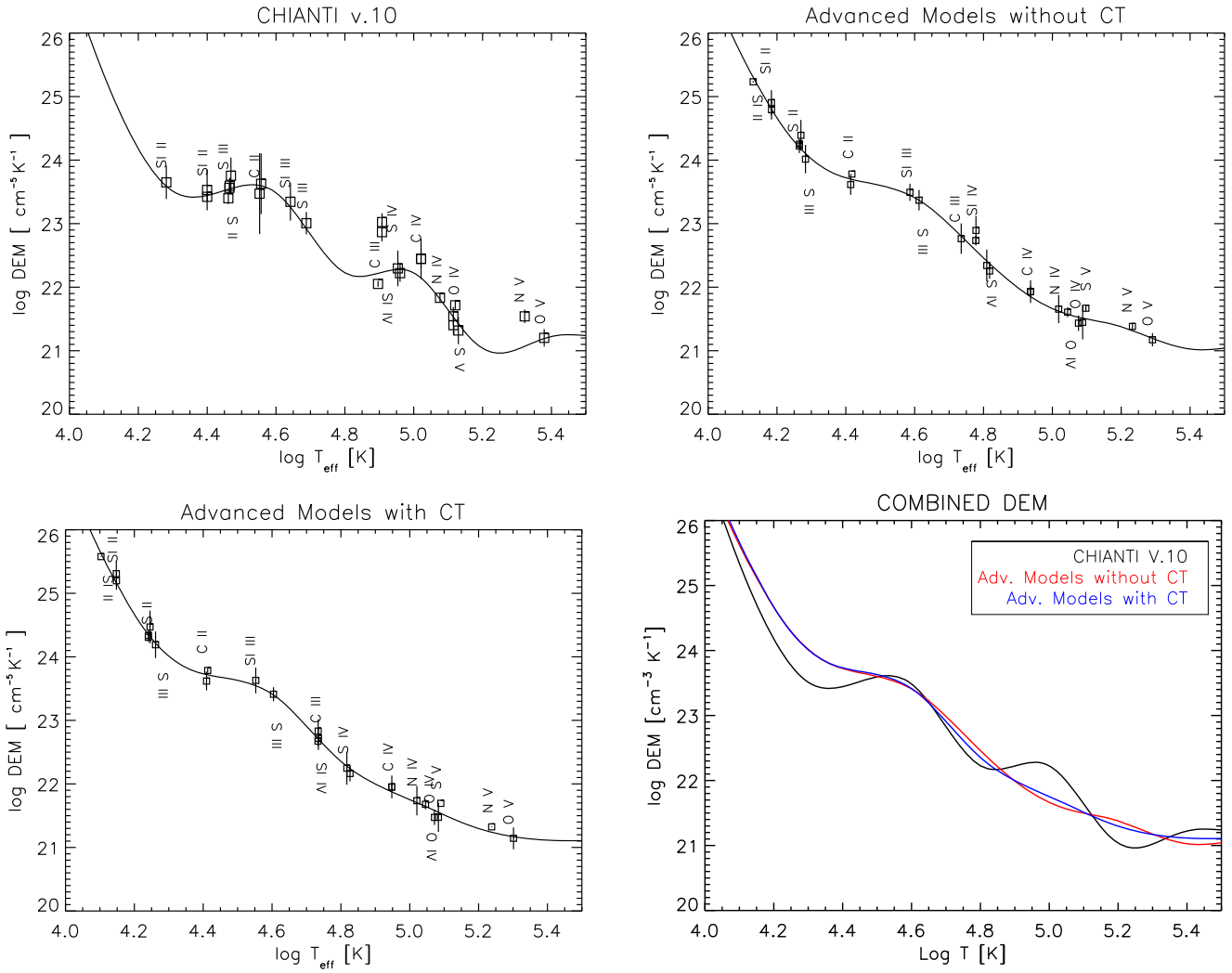

Figure 6. DEMs obtained with the three models. The points are plotted at the effective temperature, with values equal to the ratio of observed vs. predicted radiance times the DEM value at the effective temperature.

In high-density, optically thin conditions the theoretical ratio of the two C II resonance lines should be close to 2. However, it is clear that this is not the case with these observations, for which the ratio is 1.3. While the predicted to observed intensity is unchanged between all three models, it is notable that the line formation temperature decreases from 35,000 K in the coronal model to 25,700 K in the advanced models. The prediction for the Si III 1206.48 Å resonance line decreases slightly when charge transfer is included in the advanced models because the line forms at a higher temperature ($\log T_{\rm eff} = 4.55$) than where the ion fraction now peaks in the new models ($\log T_{\rm eff} = 4.45$). There is a slight increase in the predicted intensity of the S III line at 1200.94 Å because of the increase in the peak ion fraction illustrated in Figure 3.

Clearly, the biggest change in this whole work is with the Si IV resonance lines. Table 1 and Figure 5 show almost a factor of 5 increase in the intensities of the Si IV lines in the advanced model with charge transfer, and the outcome is in much better agreement with observations. In these observations, it appears the 1393.75 Å/1402.76 Å intensity ratio departs from the optically thin value of 2. It suggests opacity is not the reason for this because opacity would cause the intensity ratio to decrease below 2 as photons are absorbed from the stronger line. Gontikakis & Vial (2018) analyzed IRIS observations and found many areas in an AR where the intensity ratio is greater than 2. The majority of these cases had ratios in the range of 2.1–2.6, although they excluded significantly more cases where the signal-to-noise ratio was too low. They attribute line intensity ratios greater than the optically thin limit to resonant scattering of incident radiation in areas of lower electron density.

Figure 5 shows the much-improved ratio of the S IV lines to the O IV lines in the IRIS wavelength range. The advanced models appear to resolve the discrepancy in the ratios of these lines noted by Doschek & Mariska (2001), who limited their analysis to lines that form just above and below 10^5 K. The present atomic models may eliminate the need for the empirical correction factors used by Young et al. (2018). Improvement in this temperature range is also seen in the C III line at 1247.39 Å. Since carbon is unaffected by CT, the decrease in predicted intensity for this line in the advanced model with CT very likely comes from the effect on the DEM of the Si IV lines, which form at a similar temperature.

A notable drop is seen in the formation temperatures of the S IV lines (from 89,000 to 66,000 K); however, the predicted intensities of the S IV, N IV, O IV, and S V lines change by relatively small amounts. This highlights how, generally,

differences become smaller between the advanced models and coronal approximation for lines that form closer to the corona, as expected. Although the integrated intensities do not change so much for these ions, the O IV 1401.16 Å/S IV 1406.05 Å line ratio, which can be used as a temperature diagnostic, was shown by Rao et al. (2022) to change by factors of 2–4 when using the advanced models compared to the coronal approximation.

There are significant changes in the C IV and N V lines, which increase by factors of almost 2 and 3, respectively. They are in much better agreement with observations compared to the coronal approximation. All the anomalous ions are now well represented by the advanced models. The O V intercombination line at 1218 Å was a factor of 2 weaker than observations of the QS in Dufresne et al. (2023), yet here it is in good agreement with the plage observation. Since no other lines are used to fit the DEM at this and higher temperatures, the DEM may have adjusted to match the observation of this and the N V line, explaining why they may both be in good agreement with observations for the plage case but were not in the QS case. For the latter case, Dufresne et al. (2023) speculated that the large variability seen in observations for lines from Li- and Na-like ions imply time-dependent ionization may be required to explain their emission. Indeed, Hansteen (1993) highlighted how Li-like C IV was more affected by departures from ionization equilibrium than B-like O IV. The ionization and recombination timescales given in Section 2 are 20 times slower in the QS case, which perhaps further supports the argument that this effect may explain the discrepancies in the QS. Non-Maxwellian electron distribution functions could also affect the emission from these ions because ion formation is shifted to lower temperature with increasing departures from Maxwellian distributions, as demonstrated by Dudík et al. (2014) for Na-like Si IV. By contrast, Kerr et al. (2019) found that it would take strong flaring conditions to alter the intensity ratios of the Si IV resonance lines from the optically thin limit, indicating that radiative transfer may have a more limited impact on the emission from these ion sequences.

For ions that form at higher temperatures than HRTS was able to observe, such as Mg VII–VIII and Si VIII, the QS line intensities tested by Dufresne et al. (2023) were affected by 10%–20% using the advanced models. This also includes the Ne VII 465.2 Å line currently being observed by the SUTRI imaging mission (Bai et al. 2023); its formation temperature decreases by about 10% in the advanced models. The only higher temperature lines in the QS that showed greater variations were the Li-like O VI lines at 1031.9 and 1037.6 Å, which were enhanced by just over 40% using the advanced models. These and the Li-like Ne VIII and Na-like S VI lines cannot be tested here, but O VI and Ne VIII are currently observed by SPICE. As a whole, the models are relevant for a wide wavelength range from past and present missions, including many more lines not covered by the HRTS spectral range used as an illustration here.

3.2.4. A Note on Elemental Abundances

What is perhaps surprising when looking at the results as a whole is that good agreement is found using the photospheric elemental abundances of Asplund et al. (2021). It is often assumed in the literature that the abundances of elements with low first ionization potential (FIP), such as silicon, are greater in the atmosphere relative to the abundances of high-FIP elements, such as C, N, and O. In ARs, typical enhancements are assumed for low-FIP elements by factors between 2 and 4 relative to photospheric abundance ratios (see the reviews by Laming 2015; Del Zanna & Mason 2018). This is the so-called FIP effect. It is quite well established in quiescent ARs that high-temperature plasma around 3×10^6 K plasma has an FIP effect; the 1×10^6 K plasma in ARs has instead shown a wide range of results.

Feldman et al. (1990) used the HRTS-I observations to argue that the FIP effect is also present in the chromosphere/low transition region in an AR, where they mostly looked at Si/C intensity ratios. However, these were simply comments based on the appearance of the monochromatic images, assuming that the ions were formed at the temperatures calculated using the coronal approximation. The present work has shown clearly that assuming such temperatures is incorrect. Doschek et al. (1991) also analyzed this observation and found the same variations in the Si/C intensity ratios, but were more cautious in their conclusions.

For the specific HRTS-II plage observation used here, if the relative Si/C abundance was increased by a factor of 2–4, the Si III and Si IV lines would become over-predicted by the same amount. Sulfur has an FIP of 10 eV but in remote-sensing observations has an abundance that follows that of the high-FIP elements, depending on the conditions that lead to fractionation and the FIP effect (Laming et al. 2019). The sulfur lines in this work are generally weak but are well represented by photospheric abundances. A wider selection of lines for the TR than are available with HRTS may be required, but clearly this issue may warrant further investigation using advanced atomic models.

4. New and Updated Ions

4.1. Ne I

Details about this new addition are given in Section 2.1.

4.2. Mg VII

Young (2023) provided updated experimental energies for the $2s^2 2p^2\ ^3P_{1,2}$ and $^1D_2$ levels (indices 2–4), and the $2s2p^3\ ^3S_1$ and $^1P_1$ levels (indices 14, 15) and these have been added to the CHIANTI energy level file. The wavelengths in the radiative data file have been recomputed from the new energies.

4.3. Si VII

Young (2023) provided updated experimental energies for the $2s^2 2p^4\ ^3P_{1,0}$ levels (indices 2,3), and the $2s2p^5\ ^3P_{2,1,0}$ levels (indices 6–8), and these have been added to the CHIANTI energy level file. The wavelengths in the radiative data file have been recomputed from the new energies.

4.4. Ar V and Ar VI

The ions Ar V and Ar VI are of interest because they have been observed in SUMER spectra. They are examples of high-FIP ions and can be used to study variations of elemental abundances. The previous version of CHIANTI did not contain the ion Ar VI and the ion Ar V only included five levels in the ground configuration.

Theoretical energy levels, *A*-values, and effective collision strengths have been calculated for the argon isonuclear

sequence by Ludlow et al. (2010) and these have provided the atomic parameters for creating the new and updated models. These parameters have been supplemented by observed energy levels from Kramida et al. (2023). Wavelengths are derived from the energy levels and include "observed" wavelengths when there are NIST values for the upper and lower levels. Otherwise, the wavelengths are derived from the theoretical energies and are considered to be "unobserved." The high-temperature limits for the collision strengths are calculated from the weighted oscillator strength (*gf*-value) following Burgess & Tully (1992) with the electric dipole values provided by an AUTOSTRUCTURE calculation (Badnell 2011).

4.5. Fe XIV and Fe XV

Recently Lepson et al. (2023) have reported laboratory wavelengths of EUV lines of Fe XIV–XVI. These have allowed some new values for energies and wavelengths for Fe XIV and Fe XV but not for Fe XVI. In the case of Fe XIV, Lepson et al. (2023) identify a line at 55.152 Å that we listed as the transition $3s^25f\ ^2F_{5/2}$ to $3s^23d\ ^2D_{3/2}$ and provide an "observed" energy for the upper level. For Fe XV, they report a line at 53.10 Å that is identified as the transition between the levels $3s^2\ ^1S_0$ and $3s4p\ ^3P_1$ and a line at 46.14 Å that is identified as a transition between the $3s3p\ ^1P_1$ and $3s5s\ ^1S_0$ levels. These allow us to assign "observed" energies to the upper levels. In addition, the NIST energies for the levels $3s4f\ ^3F_2$ and $3s4f\ ^3F_3$ have been re-inserted and the value for the $3p4f\ ^3G_5$ is a new assignment.

5. Improved Radiative Recombination Energy Loss Rates

Mao et al. (2017) have used the photoionization cross sections of Badnell (2006) to derive the radiative recombination energy loss rate for ions in the H-like through Ne-like isoelectronic sequence with Z between 1 and 30. The authors provide tables of parameterized fits to the energy loss rates. These fit parameters are now included in the CHIANTI database for the appropriate ions. The greatest changes are at low temperatures where the rates of Mao et al. (2017) are considerably larger than our previous values, which relied on the Karzas & Latter (1961) free–bound Gaunt factors for levels with principal quantum numbers up to six. The Mao et al. (2017) rates include recombination to higher levels that are important at lower temperatures.

6. Conclusions

The present advanced models provide a significant change in the formation temperature of all the ions in the transition region and cause a large increase in the predicted intensities of the anomalous ions. The physics of these effects has been known for a long time, but previous models adopted more simplified atomic rates than are provided here. The present models do have different levels of approximations but are sufficient to clearly indicate where the added physical effects are most important.

An example observation is provided here to illustrate the improved agreement in the TR lines. The earlier comparison with QS observations in Dufresne et al. (2023), using the same models but with a wider selection of lines, found cases where significant discrepancies in the anomalous ions were still present. Comparisons with observations prior to that have also indicated an unclear picture, with the simple, static-atmosphere DEM models able in some cases to resolve the long-standing discrepancies for the anomalous ions. There are more factors to consider when modeling spectral lines in the transition region, such as time-dependent ionization, radiative transfer, and non-Maxwellian electron distributions. This should caution the reader that other effects are present.

The present advanced models are provided as a useful tool for any physics-based models of the solar transition region, and also as a tool for interpreting the emission from higher-density astrophysical and laboratory plasma. For example, Metcalfe et al. (2023) carried out density diagnostics of the transition region of an exoplanet host star and found similar conditions to the Sun. In their analysis, they use many of the lines for which the present models are intended, and which have shown significant variations compared to the coronal approximation.

We note that photoionization and photoexcitation can also be important effects. This affects many TR lines, altering in some cases emission in the QS from singly and doubly charged ions by factors of 2–7, such as the intercombination lines from C II and O III (Dufresne et al. 2023). These processes are also important in the outer, low-density corona. Advanced models including such processes will be included in a future CHIANTI release.

Acknowledgments

G.D.Z. and R.P.D. acknowledge support from STFC (UK) via the consolidated grants to the atomic astrophysics group at DAMTP, University of Cambridge (grant Nos. ST/X001059/1. and ST/T000481/1). P.R.Y. acknowledges support from the NASA Heliophysics Digital Resource Library. E.D. acknowledges support from STFC (UK) via a studentship. K.P.D. acknowledges support from NASA grant Nos. 80NSSC21K1785 and 80NSSC24K0119. We thank Professor Klaus Bartschat and Dr Yang Wang for providing excitation and ionization data for neutrals from their published works. The UK APAP network (PI: N. Badnell), also funded over the years by STFC, has provided a large proportion of the atomic data currently present in the database and used for advanced models.

Appendix
A Brief Summary of the Main IDL Codes and Data

A.1. IDL Routines

The main new code is called "`ch_calc_ioneq`" and is used to calculate the ion charge states for any choice of temperatures and either a fixed density or pressure. Alternatively, a grid of temperatures and related densities can be imported from a file. The subroutine "`ch_adv_model_setup`" is called to import the various parameters used throughout the calculation, including the list of ions included in the advanced model calculation (which is contained in a new file called "`advmodel_list.ions`"), and the model atmosphere parameters used for calculating charge transfer rates. The advanced models are switched on by default but can be switched off. Charge transfer is switched off by default and can be switched on by using the keyword "`ct`". Data for a few model atmospheres have been made available for the convenience of the user. As illustrated especially in Section 3 above, it is strongly advised that CT is switched on when modeling any TR ions of Si.

From this point, the ionization and recombination rates are loaded for each ion using the routine "`ch_adv_model_rates`." If available, level-resolved, direct and indirect ionization rate

coefficients are stored in files ending "`.dilvl`" and "`.ealvl`," respectively, while CT ionization and recombination rate coefficients are stored in files with suffixes "`.ctilvl`" and "`.ctrlvl`," respectively. After this, level populations are solved to form overall ionization and recombination rates and then the ion balances are solved.

A few measures have been introduced to speed up the routines. The primary one is in the calculation of the overall ionization and recombination rates, which requires the relative populations of the ground and metastable levels. For the advanced models only, the number of levels included when calculating the level populations has been reduced for some ions. In doing this, it is ensured that the populations of the metastable states are not affected by more than 2% when reducing the number of levels. The large models are mostly those that include autoionizing states, and so the optional keyword "`no_auto`" has been implemented. This removes the autoionizing states from the level population calculation since they are only relevant when modeling satellite lines in the X-rays.

The resulting ion balances are saved into a standard CHIANTI format file and used on the fly by other programs that calculate line contribution functions or intensities. Another time-saving device has been to calculate ion balances only for individual elements being modeled by the on-the-fly routines. Many existing programs have been modified to incorporate the advanced models. More details can be found in the documentation and in the headers of the programs.

A.2. Collisional Ionization Data

All the electron impact ionization data for carbon from Dufresne & Del Zanna (2019) and for oxygen from Dufresne et al. (2020) are incorporated into the current version, with one exception. A comparison of the ion balances from Dufresne & Del Zanna (2019) and the default in CHIANTI for C II shows a significant difference at low density. This arises from the ground-level ionization cross section, which is 25% higher than the experiment in Dufresne & Del Zanna (2019). For this level, CHIANTI uses the Dere (2007) cross section, which for this level was matched with the experiment of Yamada et al. (1989). Consequently, we retain the Dere (2007) cross sections for the ground level and incorporate the Dufresne & Del Zanna (2019) cross sections for the metastable levels, which were in good agreement with the *R*-Matrix calculation of Ludlow et al. (2008).

Because of the large uncertainty in using distorted wave calculations for neutrals, Dufresne & Del Zanna (2019) reduced all FAC cross sections for neutral carbon by the amount needed to bring the ground level to the experimental values at the peak. Instead of using the same method for oxygen, Dufresne et al. (2020) used the collisional ionization data for ground and metastable levels from Tayal & Zatsarinny (2016), which was in excellent agreement with the experimental results. For the CHIANTI database, other sources of neutral ionization data were investigated. Ionization cross sections from the B-spline, *R*-Matrix codes (Zatsarinny et al. 2006) are available from the excitation data currently used in CHIANTI for neutral carbon (Wang et al. 2013), nitrogen (Wang et al. 2014), neon (Zatsarinny & Bartschat 2012b), and magnesium (Barklem et al. 2017). However, when these were checked all of the ground-level cross sections were significantly below the experimental data. When the cross sections were converted to rate coefficients, differences of factors of 3 or larger at temperatures relevant for collisional ionization were found compared to the rate coefficients of Dere (2007), which were adjusted to agree with the experimental results. It is not clear whether this is because ions in metastable levels were present in the experiment, which would cause experimental values to be overestimated, or because of uncertainties in the theoretical methods. Recent calculations and experiments for ionization of, for example, neutral Ne (see Favreau et al. 2019 for a summary) have produced yet more differences. Consequently, we retain the existing methods and data from Dufresne & Del Zanna (2019) and Dufresne et al. (2021b) for ionization rates from neutrals.

A.3. Charge Transfer Data

Details of the rates and methods used for charge transfer may be found in Dufresne et al. (2021a, 2021b). The same rate coefficients have been incorporated into the current version; a summary of the sources is given below.

A.3.1. Carbon

Radiative and collisional CT rate coefficients between C I and C II come from Stancil et al. (1998a) for transitions connecting ground states, while they were derived from the cross sections in Stancil et al. (1998b) for metastable levels. For CT from the ground of C III into C II, the Errea et al. (2015) results were supplemented at low energies by the recommended cross section of Janev et al. (1988); for the metastable levels Errea et al. (2000) was used. Errea et al. (2015) results are also used for CT from C IV into C III at low energies, while Tseng & Lin (1999) results are used for higher energies. Liu et al. (2003) results are used for C V CT recombination with H and Yan et al. (2013) for reactions involving He.

A.3.2. Nitrogen

Lin et al. (2005) is used for ionization and recombination between N I and N II. Barragán et al. (2006) is used for recombination from the ground and metastable levels of N III; CT ionization out of N II is not relevant for the ion balance because it does not take place from the ground or metastable levels. For N IV, the cross sections of Bienstock et al. (1984) were supplemented at low energies by the results of Gargaud et al. (1981) in order to give rates that are relevant at the formation temperature of N III. CT with He from N IV was included using the rate coefficients of Liu et al. (2011). N V CT with H was included data obtained from Stancil et al. (1997a).

A.3.3. Oxygen

Stancil et al. (1999b) is used for transitions between the ground levels of O I and O II, and Kimura et al. (1997) for transitions involving the $2s^2\,2p^4\,{}^1D$ metastable term. Barragán et al. (2006) provide the rate coefficients for CT from O III into O II. Rate coefficients for CT with H for O IV to O III come from Wang et al. (2003); for CT with He in the same ion the results of Wu et al. (2009) are included. Lastly, the rate coefficients provided by Kingdon & Ferland (1996) are used for O V, which are derived from the calculations of Butler & Dalgarno (1980). However, these stop at a much lower temperature than where O V forms in the solar atmosphere.

A.3.4. Neon

The ionization potential of Ne I is reasonably close to He and so CT with He is the only important charge transfer process to consider. Radiative CT ionization dominates at low temperatures, and the rate coefficients from Liu et al. (2010a) for the ground level were incorporated. For collisional CT ionization of Ne I, data from Liu et al. (2010b) were supplemented with those at low energies from Zygelman & Dalgarno (1986). Zhao et al. (2006) provide radiative CT with He rate coefficients for recombination from the ground and metastable levels of Ne III. Imai et al. (2003) results are used for collisional CT and supplemented by the values from the Okuno & Kaneko experiment (as reported by Imai et al. 2003) at energies below the theoretical values. Rejoub et al. (2004) provide the cross sections from which rate coefficients were obtained for CT with H from Ne IV into Ne III.

A.3.5. Magnesium

CT rate coefficients are not available for metastable levels of Mg low-charge states and so this process has not been included in the advanced model for this element. However, the comments in Section 3.1 about its importance in the solar chromosphere should be noted.

A.3.6. Silicon

For silicon, CT ionization and recombination rate coefficients between Si I and Si II in collisions with H were obtained from Kimura et al. (1996) for both the ground and metastable terms. Clarke et al. (1998) results were used for the CT rate coefficients between Si II and Si III. For CT with H between Si III and Si IV the data come from Wang et al. (2006), while they come from Stancil et al. (1999a) for CT with He. For CT recombination with H from Si V no suitable data were found for the relevant temperature range, but Stancil et al. (1997b) results were used to incorporate rate coefficients for CT with He.

A.3.7. Sulfur

The literature on CT involving sulfur is much less extensive than for the other elements above. The only work that includes rate coefficients for the ground and metastable levels is Zhao et al. (2005b) for reactions with H between S I and Si II. Rate coefficients for CT with H from the ground of S III into S II were derived from the cross sections of Christensen & Watson (1981) and Bacchus-Montabonel & Amezian (1993), who covered different energy regimes. CT with He for these ions is covered by Zhao et al. (2005a), again just from the ground term. There are no relevant studies for CT recombination with H from S IV; for CT with He the rate coefficients from Butler & Dalgarno (1980) were used, although these are limited in temperature and the number of states included. Finally, Stancil et al. (2001) provide rate coefficients for S V in reactions with H, and Wang et al. (2002) for reactions with He.

ORCID iDs

R. P. Dufresne https://orcid.org/0000-0002-6946-4722
G. Del Zanna https://orcid.org/0000-0002-4125-0204
P. R. Young https://orcid.org/0000-0001-9034-2925
K. P. Dere https://orcid.org/0000-0003-1628-6261
E. Deliporanidou https://orcid.org/0009-0000-0209-4387
W. T. Barnes https://orcid.org/0000-0001-9642-6089
E. Landi https://orcid.org/0000-0002-9325-9884

References

Asplund, M., Amarsi, A. M., & Grevesse, N. 2021, A&A, 653, A141
Avrett, E. H., & Loeser, R. 2008, ApJS, 175, 229
Bacchus-Montabonel, M. C., & Amezian, K. 1993, ZPhyD, 25, 323
Badnell, N. R. 2006, ApJS, 167, 334
Badnell, N. R. 2011, CoPhC, 182, 1528
Badnell, N. R., O'Mullane, M. G., Summers, H. P., et al. 2003, A&A, 406, 1151
Bai, X., Tian, H., Deng, Y., et al. 2023, RAA, 23, 065014
Baliunas, S. L., & Butler, S. E. 1980, ApJL, 235, L45
Barklem, P. S., Osorio, Y., Fursa, D. V., et al. 2017, A&A, 606, A11
Barragán, P., Errea, L. F., Méndez, L., Rabadán, I., & Riera, A. 2006, ApJ, 636, 544
Bates, D. R., & McCarroll, R. 1962, AdPhy, 11, 39
Bienstock, S., Dalgarno, A., & Heil, T. G. 1984, PhRvA, 29, 2239
Brekke, P. 1993, ApJS, 87, 443
Burgess, A., & Chidichimo, M. C. 1983, MNRAS, 203, 1269
Burgess, A., & Summers, H. P. 1969, ApJ, 157, 1007
Burgess, A., & Summers, H. P. 1976, MNRAS, 174, 345
Burgess, A., & Tully, J. A. 1992, A&A, 254, 436
Burton, W. M., Jordan, C., Ridgeley, A., & Wilson, R. 1971, RSPTA, 270, 81
Butler, S. E., & Dalgarno, A. 1980, ApJ, 241, 838
Chatzikos, M., Bianchi, S., Camilloni, F., et al. 2023, RMxAA, 59, 327
Christensen, R. B., & Watson, W. D. 1981, PhRvA, 24, 1331
Clarke, N. J., Stancil, P. C., Zygelman, B., & Cooper, D. L. 1998, JPhB, 31, 533
Consortium, S., Anderson, M., Appourchaux, T., et al. 2020, A&A, 642, A14
de Pontieu, B., McIntosh, S., Hansteen, V. H., et al. 2007, PASJ, 59, S655
De Pontieu, B., Title, A. M., Lemen, J. R., et al. 2014, SoPh, 289, 2733
Del Zanna, G., Dere, K. P., Young, P. R., & Landi, E. 2021, ApJ, 909, 38
Del Zanna, G., Landini, M., & Mason, H. E. 2002, A&A, 385, 968
Del Zanna, G., & Mason, H. E. 2018, LRSP, 15, 5
Del Zanna, G., Storey, P. J., Badnell, N. R., & Andretta, V. 2020, ApJ, 898, 72
Dere, K. P. 2007, A&A, 466, 771
Dere, K. P., Del Zanna, G., Young, P. R., & Landi, E. 2023, ApJS, 268, 52
Dere, K. P., Landi, E., Mason, H. E., Monsignori Fossi, B. C., & Young, P. R. 1997, A&AS, 125, 149
Doschek, G. A., Dere, K. P., & Lund, P. A. 1991, ApJ, 381, 583
Doschek, G. A., & Mariska, J. T. 2001, ApJ, 560, 420
Doyle, J. G., Summers, H. P., & Bryans, P. 2005, A&A, 430, L29
Dudík, J., Del Zanna, G., Dzifčáková, E., Mason, H. E., & Golub, L. 2014, ApJL, 780, L12
Dufresne, R. P., & Del Zanna, G. 2019, A&A, 626, A123
Dufresne, R. P., Del Zanna, G., & Badnell, N. R. 2020, MNRAS, 497, 1443
Dufresne, R. P., Del Zanna, G., & Badnell, N. R. 2021a, MNRAS, 503, 1976
Dufresne, R. P., Del Zanna, G., & Mason, H. E. 2023, MNRAS, 521, 4696
Dufresne, R. P., Del Zanna, G., & Storey, P. J. 2021b, MNRAS, 505, 3968
Dupree, A. K. 1972, ApJ, 178, 527
Errea, L. F., Illescas, C., Jorge, A., et al. 2015, JPhCS, 576, 012002
Errea, L. F., Macías, A., Méndez, L., & Riera, A. 2000, JPhB, 33, 1369
Favreau, C. J., Johnson, C. A., Ennis, D. A., & Loch, S. D. 2019, JPhB, 52, 095203
Feldman, U., Widing, K. G., & Lund, P. A. 1990, ApJL, 364, L21
Fischer, C. F. 2005, PhRvA, 71, 042506
Fontenla, J. M., Landi, E., Snow, M., & Woods, T. 2014, SoPh, 289, 515
Froese Fischer, C., & Tachiev, G. 2004, ADNDT, 87, 1
Froese Fischer, C., Tachiev, G., Gaigalas, G., & Godefroid, M. R. 2007, CoPhC, 176, 559
Gargaud, M., Hanssen, J., McCarroll, R., & Valiron, P. 1981, JPhB, 14, 2259
Gontikakis, C., & Vial, J. C. 2018, A&A, 619, A64
Gu, M. F. 2008, CaJPh, 86, 675
Hansteen, V. 1993, ApJ, 402, 741
Imai, T., Kimura, M., Gu, J., et al. 2003, PhRvA, 68, 012716
Janev, R. K., Phaneuf, R. A., & Hunter, H. T. 1988, ADNDT, 40, 249
Jordan, C. 1969, MNRAS, 142, 501
Judge, P. G., Woods, T. N., Brekke, P., & Rottman, G. J. 1995, ApJL, 455, L85
Kambara, N., Kawate, T., Oishi, T., et al. 2021, Atoms, 9, 60
Karzas, W. J., & Latter, R. 1961, ApJS, 6, 167
Kerr, G. S., Carlsson, M., Allred, J. C., Young, P. R., & Daw, A. N. 2019, ApJ, 871, 23
Kimura, M., Gu, J. P., Hirsch, G., & Buenker, R. J. 1997, PhRvA, 55, 2778
Kimura, M., Sannigrahi, A. B., Gu, J. P., et al. 1996, ApJ, 473, 1114
Kingdon, J. B., & Ferland, G. J. 1996, ApJS, 106, 205
Kramida, A., Ralchenko, Yu., Reader, J. & NIST ASD Team 2023, NIST Atomic Spectra Database (ver. 5.11), https://physics.nist.gov/asd (Accessed: 2024 January 4)

Laming, J. M. 2015, LRSP, 12, 2
Laming, J. M., Vourlidas, A., Korendyke, C., et al. 2019, ApJ, 879, 124
Lanzafame, A. C. 1994, A&A, 287, 972
Lepson, J. K., Beiersdorfer, P., Brown, G. V., & Liedahl, D. A. 2023, ApJ, 946, 23
Lin, C. Y., Stancil, P. C., Gu, J. P., Buenker, R. J., & Kimura, M. 2005, PhRvA, 71, 062708
Liu, C.-N., Le, A.-T., & Lin, C. D. 2003, PhRvA, 68, 062702
Liu, X. J., Qu, Y. Z., Xiao, B. J., et al. 2010a, PhRvA, 81, 022717
Liu, X. J., Qu, Y. Z., Xiao, B. J., et al. 2010b, JPhB, 43, 085207
Liu, X. J., Wang, J. G., Qu, Y. Z., & Buenker, R. J. 2011, PhRvA, 84, 042706
Ludlow, J. A., Ballance, C. P., Loch, S. D., & Pindzola, M. S. 2010, JPhB, 43, 074029
Ludlow, J. A., Loch, S. D., Pindzola, M. S., et al. 2008, PhRvA, 78, 052708
Mao, J., Kaastra, J., & Badnell, N. R. 2017, A&A, 599, A10
Metcalfe, T. S., Buzasi, D., Huber, D., et al. 2023, AJ, 166, 167
Nikolić, D., Gorczyca, T. W., Korista, K. T., et al. 2018, ApJS, 237, 41
Nussbaumer, H., & Storey, P. J. 1975, A&A, 44, 321
Olluri, K., Gudiksen, B. V., & Hansteen, V. H. 2013, ApJ, 767, 43
Pietarila, A., & Judge, P. G. 2004, ApJ, 606, 1239
Rao, Y. K., Del Zanna, G., Mason, H. E., & Dufresne, R. 2022, MNRAS, 517, 1422
Rathore, B., & Carlsson, M. 2015, ApJ, 811, 80
Raymond, J. C., & Doyle, J. G. 1981, ApJ, 247, 686
Rejoub, R., Bannister, M. E., Havener, C. C., et al. 2004, PhRvA, 69, 052704
Sim, S. A., & Jordan, C. 2005, MNRAS, 361, 1102
Stancil, P. C., Clarke, N. J., Zygelman, B., & Cooper, D. L. 1999a, JPhB, 32, 1523
Stancil, P. C., Gu, J. P., Havener, C. C., et al. 1998b, JPhB, 31, 3647
Stancil, P. C., Havener, C. C., Krstić, P. S., et al. 1998a, ApJ, 502, 1006
Stancil, P. C., Schultz, D. R., Kimura, M., et al. 1999b, A&AS, 140, 225
Stancil, P. C., Turner, A. R., Cooper, D. L., et al. 2001, JPhB, 34, 2481
Stancil, P. C., Zygelman, B., Clarke, N. J., & Cooper, D. L. 1997a, JPhB, 30, 1013
Stancil, P. C., Zygelman, B., Clarke, N. J., & Cooper, D. L. 1997b, PhRvA, 55, 1064
Summers, H. P. 1974, MNRAS, 169, 663
Tayal, S., & Zatsarinny, O. 2016, PhRvA, 94, 042707
Träbert, E., Beiersdorfer, P., Brown, G. V., et al. 2022, Atoms, 10, 115
Tseng, H. C., & Lin, C. D. 1999, JPhB, 32, 5271
Vernazza, J. E., & Raymond, J. C. 1979, ApJL, 228, L89
Wang, J. G., He, B., Ning, Y., et al. 2006, PhRvA, 74, 052709
Wang, J. G., Stancil, P. C., Turner, A. R., & Cooper, D. L. 2003, PhRvA, 67, 012710
Wang, J. G., Turner, A. R., Cooper, D. L., et al. 2002, JPhB, 35, 3137
Wang, Y., Zatsarinny, O., & Bartschat, K. 2013, PhRvA, 87, 012704
Wang, Y., Zatsarinny, O., & Bartschat, K. 2014, PhRvA, 89, 062714
Wu, Y., Qi, Y. Y., Zou, S. Y., et al. 2009, PhRvA, 79, 062711
Yamada, I., Danjo, A., Hirayama, T., et al. 1989, JPSJ, 58, 1585
Yan, L. L., Wu, Y., Qu, Y. Z., Wang, J. G., & Buenker, R. J. 2013, PhRvA, 88, 022706
Young, P. R. 2023, ApJ, 958, 40
Young, P. R., Keenan, F. P., Milligan, R. O., & Peter, H. 2018, ApJ, 857, 5
Zatsarinny, O., & Bartschat, K. 2012a, PhRvA, 86, 022717
Zatsarinny, O., & Bartschat, K. 2012b, PhRvA, 85, 062710
Zatsarinny, O., Gorczyca, T. W., Fu, J., et al. 2006, A&A, 447, 379
Zhao, L. B., Stancil, P. C., Gu, J. P., et al. 2005a, PhRvA, 72, 032719
Zhao, L. B., Stancil, P. C., Gu, J. P., et al. 2005b, PhRvA, 71, 062713
Zhao, L. B., Wang, J. G., Stancil, P. C., et al. 2006, JPhB, 39, 5151
Zygelman, B., & Dalgarno, A. 1986, PhRvA, 33, 3853